

Regulate the direct-indirect electronic band gap transition by electron-phonon interaction in BaSnO₃

Binru Zhao^{1,¶}, Qing Huang^{2,¶}, Jiangtao Wu¹, Jinlong Jiao¹, Mingfang Shu¹, Gaoting Lin¹, Qiyang Sun³, Ranran Zhang⁴, Masato Hagihala⁵, Shuki Torri⁵, Guohua Wang¹, Qingyong Ren⁶, Chen Li³, Zhe Qu⁴, Haidong Zhou^{2,}, Jie Ma^{1,7,*}*

1 Key Laboratory of Artificial Structures and Quantum Control, School of Physics and Astronomy, Shanghai Jiao Tong University, Shanghai 200240, China;

2 Department of Physics and Astronomy, University of Tennessee, Knoxville, Tennessee 37996-1200, USA;

3 Materials Science and Engineering/Department of Mechanical Engineering, University of California, Riverside, California 92521, USA;

4 High Magnetic Field Laboratory, Chinese Academy of Sciences, Hefei 230031. China;

5 Institute of Materials Structure Science, High Energy Accelerator Research Organization, Tokai, Ibaraki 319-1106, Japan;

6 China Spallation Neutron Source, Institute of High Energy Physics Chinese Academy of Sciences, Dongguan 523803, China;

7 China Spallation Neutron Source, Institute of High Energy Physics Chinese Academy of Sciences, Dongguan 523803, China;

Keywords: band gap engineering, electron-phonon interaction, lattice distortion, phonon dynamic

ABSTRACT: The neutron powder diffraction, specific heat, thermal conductivity, and Raman scattering measurements were presented to study the interplays of lattice, phonons and electrons of the Sr-doping $\text{Ba}_{1-x}\text{Sr}_x\text{SnO}_3$ ($x \leq 0.1$). Although $\text{Ba}_{1-x}\text{Sr}_x\text{SnO}_3$ kept the cubic lattice, the Raman spectra suggested a dynamic distortion at low temperature. The density functional theory was applied to analyze the electronic structures and phonon dispersions of $\text{Ba}_{1-x}\text{Sr}_x\text{SnO}_3$ ($x = 0, 0.0125$), and the behaviors of electron bands around Fermi levels were discussed. According to the experimental and theoretical results, the Sr-doping played a significant role in tuning the indirect band gap of BaSnO_3 and influenced the electron-phonon interaction.

INTRODUCTION

Due to the novel physical properties, such as superconductivity, charge density wave, ferroelectricity, thermoelectricity and optical absorption,¹⁻⁵ the bulk compounds with significant electron-phonon interaction has sparked intense research upsurge in condensed matter physics^{6,7}. The charged ions from the equilibrium positions not only unbalance the local charge with the modified electrostatic potential, but also adjust the phonon excitation in the crystal.⁸ On the other hand, the increase of charge carriers could drastically improve the electrostatic screening and lower the electron-phonon interaction. Although it has been well recognized that the electron-phonon interaction

is strong in the nonmetals, the electron contribution is mainly focused and the related phonon transport has been little investigated.

The perovskite oxides, ABO_3 , could exhibit a semiconductor behavior with a wide band gap, and induce a strong impact on the lattice of the BO_6 octahedral. For instance, Barium titanate, $BaTiO_3$ (BTO), has attracted a lot of attention as a ferroelectric oxide from the off-center Ti^{4+} ions and the ferroelectric distortion has been recognized to be driven by the orbital hybridization between $3d$ states of d^0 ion Ti^{4+} and O $2p$ states.⁹ However, the localized Ti $3d$ states lead to the heavy electron effective mass, consequently limiting the carrier mobility. If the B-site Ti^{4+} ion was replaced by a large ion, Sn^{4+} ion, the first-principle calculations suggested the barium stannate, $BaSnO_3$ (BSO), to be dominantly contributed by $2s$ states of s^0 ion Sn^{4+} with the small effective mass and result in a low electron density-of-states with an indirect gap of 3.1 eV. Meanwhile, BSO is cubic at room temperature, Fig. 1(a).

BSO exhibits a wide doping tunability from the high symmetric lattice structure, while the A-site substitution could adjust the environment of BO_6 octahedral and induce lattice distortion to effectively tune the optical property. In order to explore the unique property of BSO, the Sr ion is introduced on the Ba-site. Sr is in the same II_A group as Ba, while the atomic radius is a trifle smaller than that of Ba atom. $SrSnO_3$ (SSO) is similar as BSO, such as the low electron effective mass¹⁰⁻¹², and the indirect band gap of 4.0 eV¹³ suggests enhanced bond energy and the localized electrons. Hence, Sr replacement to Ba cations induce the strong ionic size effect on the band structure and

electron-phonon coupling.

In this work, we presented a systematic illustration of the structural and thermal properties of $\text{Ba}_{1-x}\text{Sr}_x\text{SnO}_3$ ceramics (BSSOs, $x = 0, 0.03, 0.06, 0.1$), viz. the lattice parameters, heat capacity, thermal conductivity and Raman shift, as the function of Sr substitution and temperature. Combining the simulations of the phonon dispersion and the electronic band structures of $\text{Ba}_{1-x}\text{Sr}_x\text{SnO}_3$ ($x = 0, 0.125$), not only the lattice vibrations and electronic structures had been analyzed in details, but the strong electron-phonon interaction had been discussed.

RESULTS AND DISCUSSION

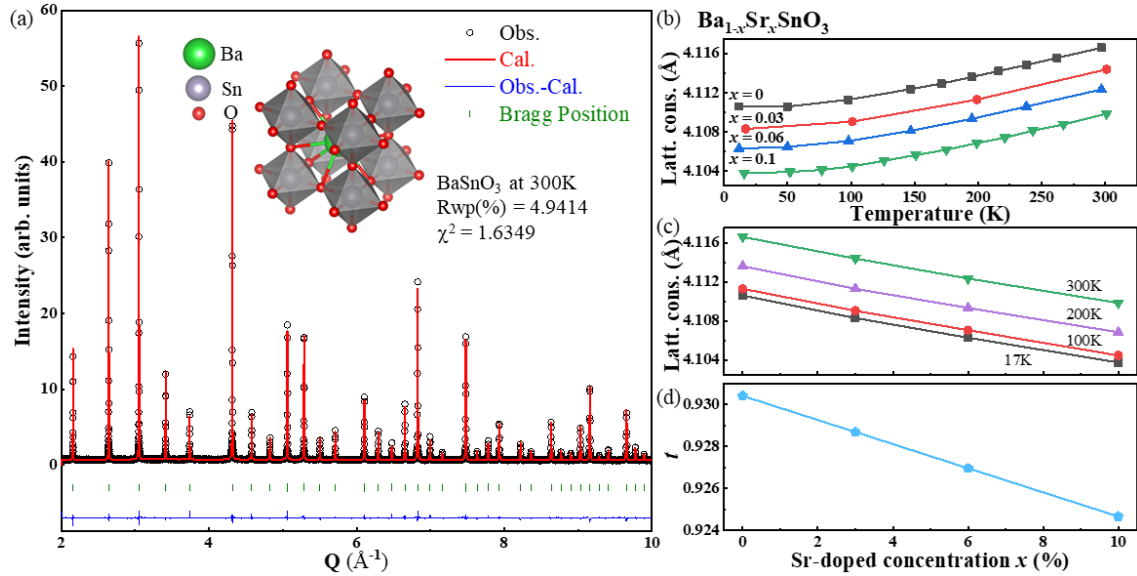


Figure 1. (a) Neutron powder diffraction pattern and simulation of BaSnO_3 at 300 K. (b) and (c) Temperature- and Sr-doping-dependence of the lattice parameters of BSSOs, respectively. (d) The Goldschmidt tolerance factor t as a function of Sr-doped concentration at 300 K.

Neutron Powder Diffraction. Figure 1 (a) presented the comparison of Neutron powder diffraction (NPD) data and Rietveld refinement of BSO at 300 K with a space group $Pm\bar{3}m$. The lattice parameters as a function of temperature and Sr-doped concentration were shown in Figure 1 (b) and (c), respectively. As the temperature increased, the lattice parameters of BSSO monotonically increased. Meanwhile, the lattice constants decreased with the increase of Sr-content due to the smaller radius of Sr^{2+} ion than that of Ba^{2+} ion. The lowest lattice parameter was 4.104 Å in $Ba_{0.9}Sr_{0.1}SnO_3$ at 17 K.

The Goldschmidt tolerance factor, t , was used to predict the stability of the perovskite structure, ABO_3 ,

$$t = \frac{r_A + r_O}{\sqrt{2}(r_B + r_O)} \quad (1)$$

where r_A , r_B , r_O were the ionic radius.

The ionic radius of Sn^{4+} and O^{2-} ions were 69 and 140 pm, respectively, and the ionic radius on A-site referred to the combination of Ba^{2+} (135 pm) and Sr^{2+} (118 pm) ions. The values of t were obtained by weighted average in doping compounds.¹⁴ Compared to 1 for the ideal cubic structure, $t(BSO)$ was 0.93 and the polar distortion or oxygen octahedra tilting was observed. As the smaller Sr-ion substituted the Ba-ion, the lattice distortion increased with a lower t and both bond lengths of (Ba, Sr)-O and Sn-O decrease, which increased the interaction between A-site (Ba, Sr) and Sn cations.

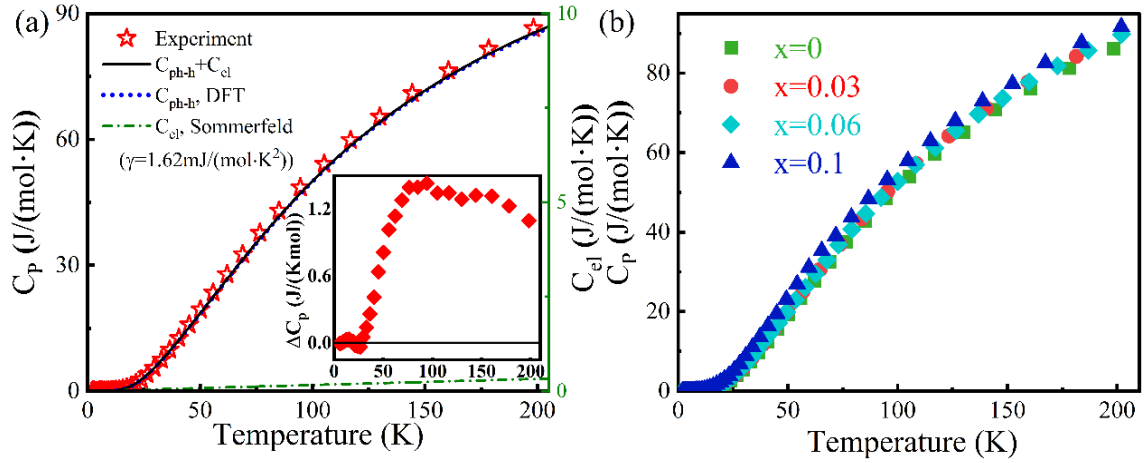


Figure 2. (a) The heat capacity C_p of BaSnO_3 . The C_{ph-DFT} of harmonic phonons is calculated by *phonopy* and C_{el} is the electron heat capacity in Sommerfeld approximation. (b) C_{PS} of BSSOs from 2 K to 200 K.

Specific Heat. The specific heats, C_{PS} , of the BSSOs were measured from 2 to 200 K and agreed with the calculations well, Fig. 2. The electronic specific heat, C_{el} , was estimated by the Sommerfeld Theory, *i. e.* $C_{el} = \gamma_{el}T$, where γ_{el} was the Sommerfeld parameter as $1.62 \text{ mJ}/(\text{mol}\cdot\text{K}^2)$ for BSO.

To investigate the lattice specific heat, C_{ph} , we calculated the specific heat of harmonic phonon, C_{ph-h} , by the *phonopy* code on density function theory (DFT) and estimated the anharmonic effect, C_{ph-an} , qualitatively. C_{ph-h} did not depend on volume and temperature, $C_{ph-h,V} = C_{ph-h,P}$, while C_{ph-an} depended on both factors of volume and temperature. Therefore, the difference of $\Delta C_p = C_p - C_{ph-h} - C_{el}$ was mainly described as C_{ph-an} , the inset of Fig. 2(a), which was started to be observed around 40 K. Above 100 K, ΔC_p gradually decreased for the Dulong-petit theory limitation, $3nR$, where $n = 5$ was the atomic number per formula and the molar gas constant $R = 8.31 \text{ J}/(\text{mol}\cdot\text{K})$.

Figure 2(b) was the C_{Ps} of BSSOs from 2 K to 200 K, and the Sr^{2+} -content induced to a higher C_P by enhancing the lattice distortion and introducing the impurity-anharmonicity term, $C_{ph-Im,A}$. Moreover, the C_P difference between Sr-doped BSO and the parent compound was less than 3% at high temperature due to the Dulong-Petit limitation. The lattice dynamics would be discussed in details in the section of the Raman spectra to explain this anomaly.

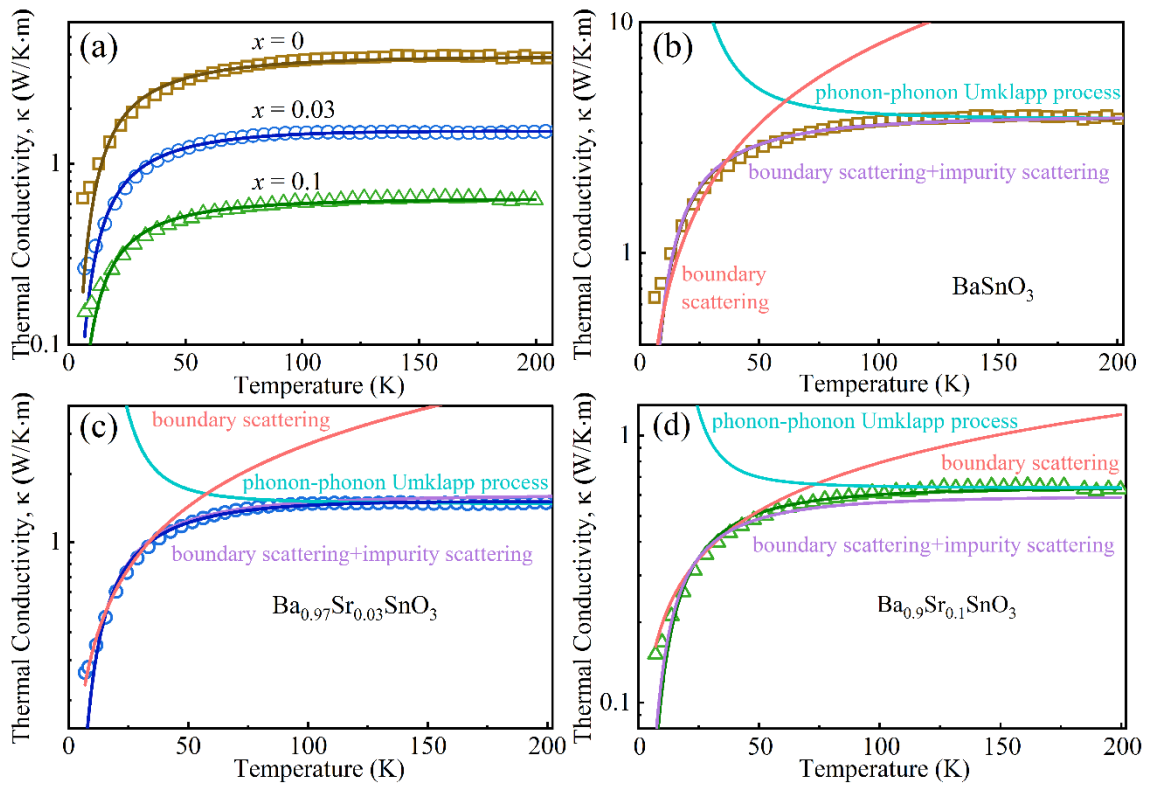


Figure 3. (a) The thermal conductivities κ s of $\text{Ba}_{1-x}\text{Sr}_x\text{SnO}_3$ ($x = 0, 0.03, 0.1$) in the temperature range 20 K-300 K. (b)-(d) The thermal conductivities contributed by boundary scattering $\kappa_b \sim T^3$, impurity scattering described by the part of Debye-Callaway model and Umklapp process $\kappa_U \sim A \exp(-\Theta_D/3x) T^{-2}$.

Thermal Conductivity. Figure 3 presented the thermal conductivity, κ , of BSSOs. Due to the wide band gap of BSO,¹⁵ κ was mostly contributed by the lattice and was

gradually flattened above around 100 K. In order to obtain different contributions of the lattice thermal conductivity, and the nonmagnetic simplified Debye-Callaway model¹⁶ based on Boltzmann distribution was applied,

$$\kappa_{lattice} = \frac{k_B}{2\pi^2 v_{ph}} \left(\frac{k_B T}{\hbar} \right)^3 \int_0^{\theta_D/T} \frac{\tau_{ph} x^4 e^x}{(e^x - 1)^2} dx \quad (2)$$

$$\frac{1}{\tau_{ph}} = \frac{1}{\tau_U} + \frac{1}{\tau_b} + \frac{1}{\tau_i} \quad (3)$$

$$\frac{1}{v_{ph}} = \frac{1}{3} \left(\frac{2}{v_t} + \frac{1}{v_l} \right) \quad (4)$$

where $x = \hbar\omega/k_B T$, and θ_D was the Debye temperature. τ_{ph} was the phonon relaxation time which affected by the Umklapp process (τ_U), boundary scattering (τ_b) and impurity scattering (τ_i) including both mass-difference scattering and dislocation scattering. v_t , v_l , and v_{ph} were the transverse, longitudinal and average sound velocities, respectively.

The mean lifetime of boundary scattering was expressed as $\tau_b^{-1} = v_{ph}/L$ with the grain size (L) for the polycrystal. The phonon-phonon Umklapp process relaxation time was $\tau_U^{-1} = BT^3\omega^2 e^{-\theta_D/3T}$ for the insulators, and both B and b were fitted by the experiment data. The phonon relaxation time of impurity scattering was $\tau_i^{-1} = A\omega^4$. For the Sr-doped BSO, the impurity term was modified by Klemens¹⁷:

$$A = \frac{V}{4\pi v_s^3} \cdot \Gamma \quad (5)$$

$$\Gamma = \Gamma_{MF} + \Gamma_{SF} \quad (6)$$

where V was the volume per atom, Γ included the disorder induced by mass difference fluctuation (Γ_{MF}) and strain field fluctuation (Γ_{SF}) by dislocation.

The lattice distortion of the different atomic sizes at *A*-site and interatomic force field caused by the host atom would further scatter the phonon.¹⁸

$$\Gamma_{MF} = \frac{1}{3}x(1-x) \left(\frac{M_{Ba} - M_{Sr}}{M_{aver}} \right)^2 \quad (7)$$

$$\Gamma_{SF} = \frac{1}{3}x(1-x) \varepsilon \left[\frac{(1-x)M_{Ba} + xM_{Sr}}{M_{aver}} \right]^2 \left[\frac{r_{Ba} - r_{Sr}}{xr_{Sr} + (1-x)r_{Ba}} \right]^2 \quad (8)$$

where M_{Ba} , M_{Sr} , M_{aver} represented the masses of Ba and Sr ions and the average ionic mass in one primitive cell, respectively. x meant the substituted fraction, ε was the adjustable parameter in the range of 10 to 100 for the Sr sublattice¹⁸, r_{Ba} and r_{Sr} were the atomic radius of Ba and Sr, respectively.

As shown in Fig. 3(b)-(d), the crystal grain boundary mainly scattered the phonons at low temperatures, while the contribution of impurity should be included with the increasing temperature. Finally, the U-process flattened the curve at high temperatures by reinforcing the anharmonic phonon-phonon interaction.

Table 1. Γ_{MF} , Γ_{SF} and ε were combined the impurity scattering coefficient and resulted in the parameter A in Eq.5. B was the Umklapp scattering coefficient and b was the Umklapp scattering temperature coefficient. v/L represented the boundary scattering.

Configuration	Γ_{MF}	Γ_{SF}	ε	$A(s^3)$	$B(s^2/K)$	$v/L(m/s^2)$
BaSnO ₃	-	-	-	6.17×10^{-42}	1.6×10^{-33}	8.73×10^9
Ba _{0.97} Sr _{0.03} SnO ₃	0.01	0.10	84.80	1.91×10^{-41}	9.9×10^{-32}	2.45×10^{10}
Ba _{0.9} Sr _{0.1} SnO ₃	0.03	0.24	69.57	6.25×10^{-41}	1.0×10^{-33}	5.70×10^{10}

As the Sr concentration increased, the thermal conductivity was reduced. The disorder coefficients Γ_{MF} and Γ_{SF} were listed in Table 1: the replacement of the

lighter/smaller Sr ions not only led to the interaction between Ba and Sr atoms on Eq. (7) by the mass difference, but also enhanced the lattice distortion by the strain field including the SnO₆ octahedra. Additionally, the contribution from mass difference and strain field were variable in doped compounds. For Ba_{0.97}Sr_{0.03}SnO₃ configuration, Γ_{MF} and Γ_{SF} had same magnitude, suggesting the comparable contributions from the mass difference and strain field. However, Γ_{MF} was significantly larger than Γ_{SF} in the doped compounds. Which we mentioned above demonstrated that the lattice distortion from the strain field played an important role to scatter phonons due to the Sr substitution. Above around 100 K, the combination of impurity scattering, phonon-phonon scattering, phonon-boundary scattering and potential electron-phonon coupling simultaneously affected the lattice thermal conductivity and introduced the flat κ .

Table 2. Frequencies (cm⁻¹) of Raman peaks in experiment, compared with the calculated phonon modes of BaSnO₃ at the high symmetry points R, M, Γ and in Pbnm structure. The star symbol * represented the second-order Raman mode.

Raman data	Phonon mode	R $\bar{3}c$	P4/mbm	Pbnm	Γ (0,0,0)
		R (0.5,0.5,0.5)	M ₁ (0.5,0.5,0)		
266	TO ₂			260	248
278	TO ₂	275			
286	TO ₂		288		
299	LO ₂			292	
357	LO ₂	344			384
479	2TO ₂ *				
527	TO ₃		522		
553	TO ₃			553	
595	TO ₃			579	
610	TO ₃			596	
629	TO ₃				645
657	TO ₃		656		

Raman Spectra. To further investigate the intrinsic phonon behavior, the temperature dependent Raman spectra of $\text{Ba}_{1-x}\text{Sr}_x\text{SnO}_3$ ($x = 0, 0.03, 0.06, \text{ and } 0.1$) were measured at the Steady High Magnetic Field Facility, Hefei, China. Fig. 4 presented the Raman spectra of the parent compound BSO. With the increasing temperature, the Raman excitations merged together and the number of Raman active modes decreased (see Fig. 4(a)). Especially, a “transient state” was demonstrated as the excitations slightly converged together in the range of 69.5 - 101 K¹⁹. Meanwhile, the excitations at 357, 527 and 657 cm^{-1} disappeared and the excitation at 409 cm^{-1} appeared around 69.5 K. Since the Raman active mode should not be observed in the ideal cubic lattice structure with the space group $\text{Pm}\bar{3}\text{m}$, the Raman modes at 5.6 K suggested the lowered lattice symmetry caused by a potential lattice distortion.

The phonon dispersions and partial density of states of BSO were simulated by *phonopy* code with linear response method, Fig.4(c) and (d). The LO-TO splitting induced by electrostatic potential in nonmetals was considered. The optical modes in the frequency range of 150 - 425 cm^{-1} were contributed by the distorted SnO_6 octahedra. The high energy scale, above 500 cm^{-1} , primarily related to the O-O modes. The phonon frequency 480 cm^{-1} was located in the band gap and regarded as second-order Raman modes. The longitudinal (LO) and transverse (TO) optical phonon modes were selected to analyze the phonon behavior, Table 2. According to the group theory and transition rule, the phonon states transformed from $\text{Pm}\bar{3}\text{m}$ to tetragonal $\text{P4}/\text{mbm}$ ²⁰, orthorhombic Pbnm or even rhombohedral $\text{R}\bar{3}\text{c}$ could explain the observed discrepancy between the

theory and experiment.²¹ The lattice distortion shifted zone-center to M₁- or R-point from Pm $\bar{3}$ m to P4/mbm or R $\bar{3}$ c, respectively. To examine the Raman modes of BSO with the space group Pbnm, the harmonic lattice vibrations were assumed at 5.6 K. In the harmonic approximation with the fixed force constant, the relation of the masses and frequencies of BSO and SSO within the same structure was shown in the following equation²²:

$$\frac{\nu_{Ba}}{\nu_{Sr}} \approx \sqrt{\frac{M_{Sr}}{M_{Ba}}} \quad (9)$$

where ν and M were the vibration frequency and atomic mass, respectively.

Thus, it was obvious that the zone-center phonon shift to M- or R- points in FBZ and a lattice distortion from dynamic phase transition was occurred in the undoped BSO.

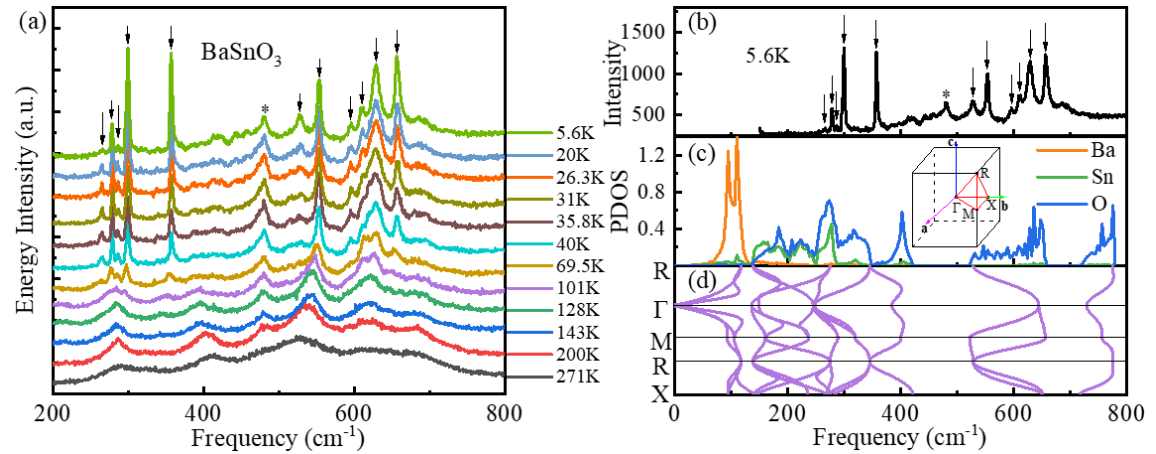


Figure 4. (a) Temperature dependence of the Raman spectrum of BaSnO₃. (b) The Raman spectrum of BaSnO₃ at 5.6 K. (c) and (d) The calculated partial density states and phonon dispersion of BaSnO₃, respectively. The inset in (c) indicated the high symmetry points in the FBZ.

Sr-doping affected the Sn-O and O-O vibrations indirectly by varying the

environment of the SnO₆ octahedra, and the related effect on the lattice vibrations was obtained from the temperature-dependence of BSSOs, Fig.5. i) The Raman mode at 357 cm⁻¹ was the excitation at the zone boundary, *R*-point, and was responsible for the O-O bond. This mode had no significant change with low-concentration Sr doping at 5.6 K, whereas, the Sr²⁺-ion substituting constructed the asymmetric coordination environment and distorted the lattice, corresponding to the phonons moving to the zone center from the zone boundary, i.e. M or R points. However, *R*-point phonons was not observed at 300 K, Fig. 5. ii) Both Raman active modes at 528 and 610 cm⁻¹ were the excitations of the O-O bonds. The redshift was observed at 300 K while the blueshift was presented at 5.6 K. Hence, the O-O vibration was determined by the competition of the low-fraction doping on the lattice distortion and the thermal effect on the lattice symmetry. Moreover, those broad and asymmetry excitations ruled out that Sr doping strengthened the O-O polarizability. iii) The Raman active mode at 629 cm⁻¹ was contributed by both Sn-O and O-O modes, and demonstrated that Sr-substitution enhanced the distortion of SnO₆ octahedra. Furthermore, this phonon excitation was not observed at 300 K and suggested that the lattice distortion was less at high temperature.

To further understand the lattice distortion and quantitatively describe the phase transition temperature in BSSO, the temperature-dependence of Raman shifts were presented in Fig. 5(j)-(l). Firstly, the temperature dependence of Raman shifts could be simply described²³

$$\omega = \omega_0 - \alpha_1 T - \alpha_2 T^2 \quad (10)$$

where ω_0 was the excitation at 0 K, α_1 and α_2 were the first- and second-order temperature coefficients, respectively.

The wavenumbers could be obtained from the combination of lattice and phonon-phonon anharmonic terms as the decay of two phonons ω_1 and ω_2 , and three identical phonons of $\omega/3$ ²⁴:

$$\omega = \omega_0 + A \left(1 + \frac{1}{e^{x_1} - 1} + \frac{1}{e^{x_2} - 1} \right) + B \left(1 + \frac{3}{e^{x_3} - 1} + \frac{3}{(e^{x_3} - 1)^2} \right) \quad (11)$$

where $x_1 = \hbar\omega_1/k_B T$, $x_2 = \hbar\omega_2/k_B T$, $x_3 = \hbar\omega_3/k_B T$. The parameters A and B were the third and fourth order decay, respectively. \hbar , k_B and T denoted the Planck's constant, the Boltzmann's constant and the temperature, respectively. The frequency ω_0 was obtained by Eq. (14).

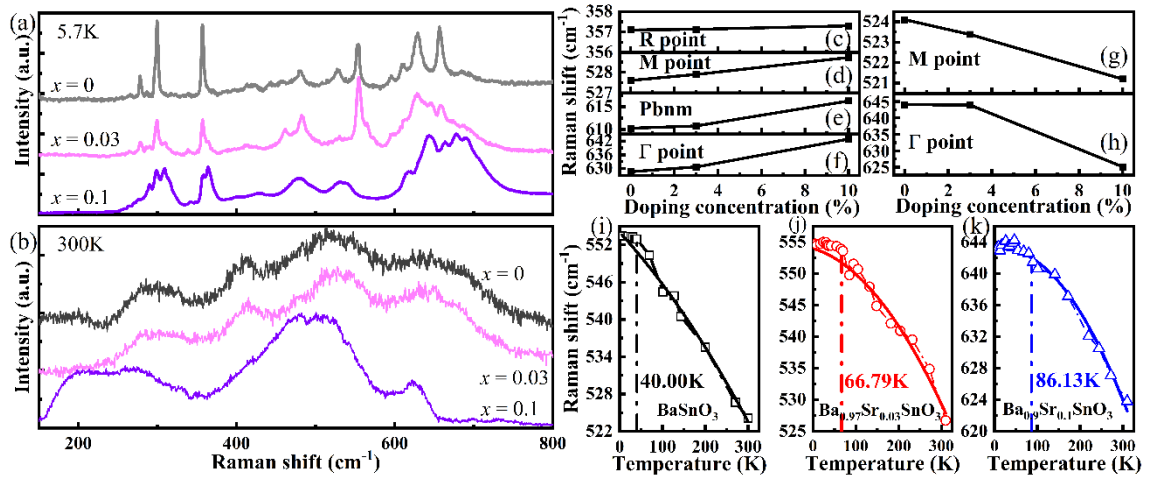


Figure 5. The Raman spectra of $\text{Ba}_{1-x}\text{Sr}_x\text{SnO}_3$ ($x = 0, 0.03, 0.1$) at 5.7 K(a) and 300 K(b). (c)-(h) Composition-dependence of some intense frequencies for $\text{Ba}_{1-x}\text{Sr}_x\text{SnO}_3$ ($x = 0, 0.03, 0.1$) at 5.6 K and 300 K. The temperature-dependence of the Raman excitations of (i) BaSnO_3 , (j) $\text{Ba}_{0.97}\text{Sr}_{0.03}\text{SnO}_3$, (k) $\text{Ba}_{0.9}\text{Sr}_{0.1}\text{SnO}_3$.

The temperature-dependence of 554 cm^{-1} (TO_3) for BSO corresponded to O-O polarization, Fig. 5(i), and an anomaly was observed around 40 K, which not only suggested a lattice distortion on the Raman active mode, but also agreed with the heat capacity of BSO, inset Fig. 2(a). In the cases of $\text{Ba}_{0.97}\text{Sr}_{0.03}\text{SnO}_3$, Fig. 5(j), the phase transition temperature increased to 66.79 K. The Raman mode at 644 cm^{-1} was originated from the tortuosity of Sn-O octahedra and O-O polarization for $\text{Ba}_{0.9}\text{Sr}_{0.1}\text{SnO}_3$, Fig. 5(k), and the transition temperature was around 86.13 K. Therefore, the Sr doping strengthened the bond energy and lattice distortion to zone boundary.

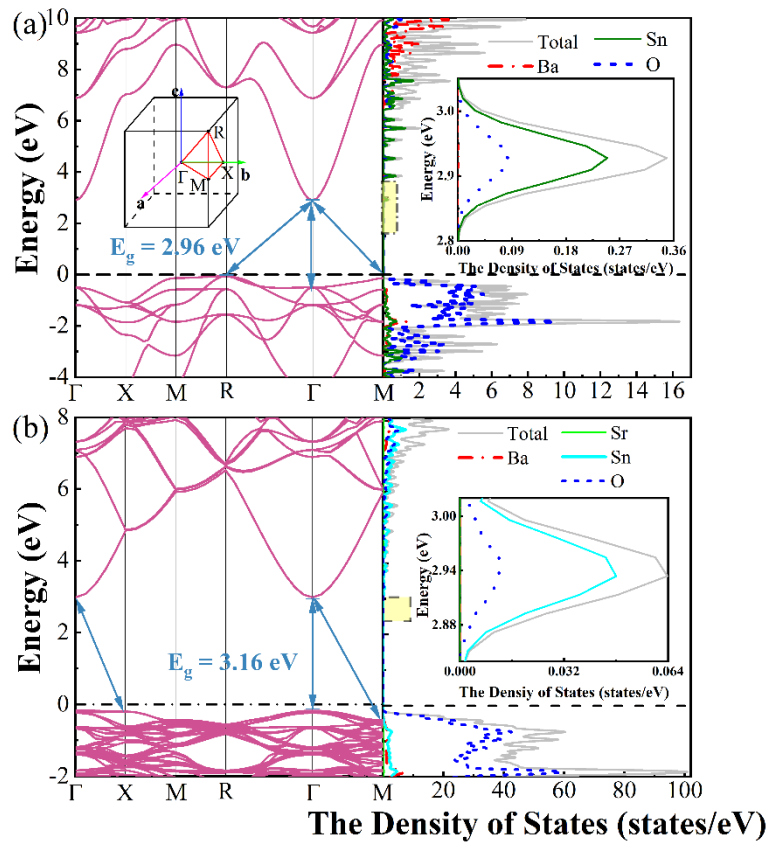


Figure 6. The band structure and total density of states of BaSnO_3 in unit cell (a) and $\text{Ba}_{0.875}\text{Sr}_{0.125}\text{SnO}_3$ in $2\times 2\times 2$ supercell (b), respectively. Fermi levels were described by black dash line.

Electronic structures of $\text{Ba}_{1-x}\text{Sr}_x\text{SnO}_3$ ($x = 0, 0.125$). The electronic properties of $\text{Ba}_{1-x}\text{Sr}_x\text{SnO}_3$ ($x = 0, 0.125$) were discussed theoretically through the band structures, total and partial density of states using HSE06 hybrid functional calculation. The lattice parameter of the optimized structure of BaSnO_3 was 4.10 \AA as the NPD experiment. In Fig. 6 (a), the conduction band minimum (CBM) and valence band maximum (VBM) located at Γ and R points, respectively, and the indirect band gap was 2.96 eV , which was consistent with the experiment results $2.93\text{-}3.4 \text{ eV}$, Table 3.^{15, 25} The total density of states (TDOSs) indicated that Sn and O atoms mainly contributed to the conduction and valence band, respectively. The DOS of Ba atoms was much smaller in both bands, while the electrons located at s orbit primarily formed the Sn states, and the electrons dominating p orbits offered the foremost contribution to the O states just below Fermi energy (see in Fig. 7).

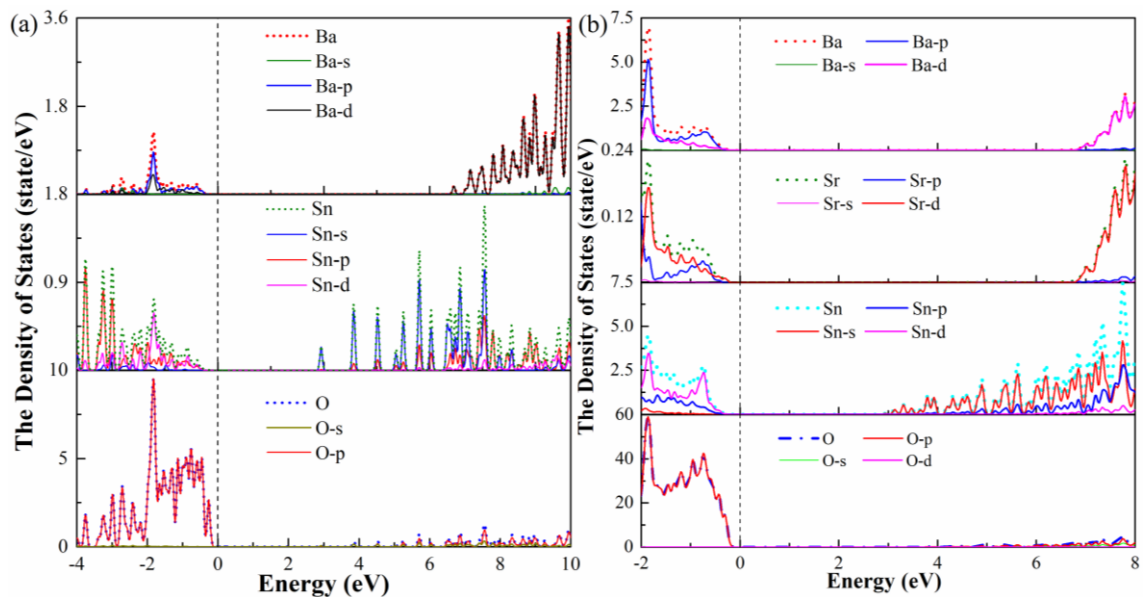


Figure 7. The partial density of states of BaSnO_3 in unit cell (a) and $\text{Ba}_{0.875}\text{Sr}_{0.125}\text{SnO}_3$ in $2 \times 2 \times 2$ supercell (b), respectively. Fermi levels were described by black dash line.

For $\text{Ba}_{0.875}\text{Sr}_{0.125}\text{SnO}_3$, $2 \times 2 \times 2$ supercell was applied and the lattice parameter was 4.08 Å. Significantly changes in the band structures of CBM and VBM were obtained at the Γ point by Sr substitution. The electron was removed from the Fermi energy by a large bandgap energy of 3.16 eV, and the indirect band gap was tuned to the direct band gap as the distorted BaSnO_3 .²⁰ Hence, the Sr-doping induced the zone center to M or R points and valence electrons near the Fermi surface transferred to the Γ or X points, Table 3.

Compared to the Raman excitations with the Sr-doping, the electron-phonon coupling was clearly broken and the energy gap became large for a stable structure. This similar feature was obtained in $\text{Ba}_{0.75}\text{Sr}_{0.25}\text{SnO}_3$ and $\text{Ba}_{0.25}\text{Sr}_{0.75}\text{SnO}_3$, Table 3.²³ For SSO, the lattice is pseudo-cubic with the space group Pbnm and the electron band was back to an indirect one as 3.95 eV. Hence, we offered an effective approach to improve the optical properties of BSO and essentially illustrate the reason for the migration of electron and phonon behavior.

Table 3. The band gaps (in eV) along different electronic excitation paths. The symbol \blacklozenge labeled the energy gap from VBM to CBM.

Configuration	$\Gamma \rightarrow \Gamma$	X \rightarrow Γ	M \rightarrow Γ	R \rightarrow Γ
BaSnO_3	3.40	3.95	3.10	2.96 \blacklozenge
$\text{Ba}_{0.875}\text{Sr}_{0.125}\text{SnO}_3$	3.16 \blacklozenge	3.19	3.42	3.53
$\text{Ba}_{0.75}\text{Sr}_{0.25}\text{SnO}_3$	3.22 \blacklozenge	3.25	3.53	3.62
$\text{Ba}_{0.25}\text{Sr}_{0.75}\text{SnO}_3$	3.83	4.00	3.74 \blacklozenge	3.99

In Fig. 6, CBM and VBM were dominated by Sn and O atoms, respectively, and O states moved away from the Fermi level to enlarge the energy gap by doping Sr-ions. To further understand the role of each orbital, PDOS of $\text{Ba}_{0.875}\text{Sr}_{0.125}\text{SnO}_3$ was simulated, Fig. 7, and the Ba and Sr states near the Fermi energy were from the electrons occupying p and d orbitals, respectively. The bottom of the conduction region and top of the valence region was contributed by Sn-s and O-p orbitals, respectively.

CONCLUSION

In summary, we systematically investigated the structural, thermal properties and electronic structures of Sr-doped BSO ceramics. The temperature-dependence Raman spectra revealed that the intrinsic lattice distortion in the undoped BSO activated the Raman modes and induced zone-center phonon shifted to zone boundary, finally, a potential dynamic phase transition occurred as the temperature increased. The electrons below the Fermi level located at M or R points and could interact with the moved phonons, which enhanced the anharmonic effect. Sr doping strengthened the lattice distortion and lowered the phonon symmetry. In contrast, the electron below the Fermi energy moved to Γ point and the conduction band minimum always located at Γ point, resulting in the direct band gap. Thus, Sr doping could tune the indirect band gap to direct band gap and break the electron-phonon coupling. Finally, the gap energy became larger in order to lower energy states.

EXPERIMENTAL AND THEORETICAL DETAILS

Synthesis of $\text{Ba}_{1-x}\text{Sr}_x\text{SnO}_3$. The precursors of BaCO_3 (99.97%), SrCO_3 (99.9%), and SnO_2 (99.9%) were used to synthesize the polycrystalline samples of $\text{Ba}_{1-x}\text{Sr}_x\text{SnO}_3$ with $x = 0, 0.03, 0.06, 0.1$ via solid state reaction.

Neutron powder diffraction. The neutron powder diffraction (NPD) of $\text{Ba}_{1-x}\text{Sr}_x\text{SnO}_3$ were taken on BL08 Super High Resolution Powder Diffractometer time-of-flight diffractometer (SuperHRPD) at the Material and Life Science Facility of Japan Proton Accelerator Research Complex (J-PARC). The diffraction datum was collected at the various temperature ranging from 10 K to 300 K and the Rietveld refinement was performed by the Z-Rietveld software.

Physical properties. The heat capacity and the thermal conductivity were carried out by the Physical Property Measurement System (PPMS).

The temperature dependent Raman spectra of $\text{Ba}_{1-x}\text{Sr}_x\text{SnO}_3$ were obtained by the DXR Raman Microscope (Horiba JY T64000) with the laser of 532.1 nm and a Janis ST-500 microscopy cryostat down to 5.6 K. The scanning range was from 150-800 cm^{-1} with the resolution 0.5 cm^{-1} and the data were recorded by the charged-coupled device (CCD) of single exposure.

First-principles calculation. The calculations were performed by the first-principles analysis based on density functional theory (DFT) as implemented in the Vienna *Ab initio* Simulation Package (VASP)^{26, 27}. The ion-electron interactions were approximated using the projected-augmented plane method (PAW)²⁸, and the local density approximation (LDA) in the form of Ceperley-Alder-Perdew-Zunger (CAPZ)

parameterization^{28, 29} was employed to simulate the electron-exchange correlation potentials. The plane wave basis with a cutoff energy of 500 eV was used.

To investigate the influence of Sr doping on the electronic structures of BaSnO₃, we selected a 2×2×2 supercell containing a whole number of 40 atoms whereas one Ba atom was substituted by one Sr atom to insightfully observe the effect of 12.5% Sr-doped concentration. The integrations over the bulk Brillouin zone of the BaSnO₃ unit cell and the 2×2×2 supercell of Ba_{0.875}Sr_{0.125}SnO₃ were calculated by the Monkhost-Pack special k meshes 9×9×9 and 7×7×7, respectively. In order to the full structural optimization, the energy and force convergence standard for each atom were set to 10⁻⁷ eV and 0.01eV/Å, respectively. We utilized the Hartree-Fock/DFT hybrid functional³⁰ with the range-separation parameter of 0.2 Å⁻¹ to obtain the accurate band structures³¹⁻³³ and the default fraction of exact exchange was 25%. The valence electronic configuration of Ba and Sr atoms was 5s²5p⁶6s² and 4s²4p⁶5s², respectively. Ba²⁺ and Sr²⁺ cations were generated in Ba_{1-x}Sr_xSnO₃. For Sn atom, the electrons occupying the 5s² and 5p² orbits were taken in valence. The valence electrons of O atom were 6 (2s²2p⁴).

The phonon behavior of BaSnO₃ was calculated through *phonopy* code based on DFT. We enlarged the primitive cell to the 4×4×4 supercell for the computation of phonon dispersion, PDOSs and specific heat. The Gamma-centered k-point grids were selected as 5×5×5 and the energy convergence was set to 10⁻⁹ eV.

AUTHOR INFORMATION

Corresponding Authors

Haidong Zhou – *Department of Physics and Astronomy, University of Tennessee, Knoxville, Tennessee 37996-1200, USA; Email: hzhou10@utk.edu*

Jie Ma - *Key Laboratory of Artificial Structures and Quantum Control, School of Physics and Astronomy, Shanghai Jiao Tong University, Shanghai 200240, China; Wuhan National High Magnetic Field Center, Huazhong University of Science and Technology, Wuhan 430074, China; Email: jma3@sjtu.edu.cn*

Author Contributions

[†]B.R.Z. and Q.H. contributed equally.

Notes

The authors declare no competing financial interest.

ACKNOWLEDGMENTS

B.R.Z., J.T.W., J.L.J., M.F.S., G.T.L., G.H.W., Q.Y.R and J.M. acknowledge the financial support from the National Science Foundation of China (Nos. 11774223, and U2032213), the interdisciplinary program Wuhan National High Magnetic Field Center (Grant No. WHMFC 202122), Huazhong University of Science and Technology. The

work at the University of Tennessee (Q.H., and H.D.Z.) was supported by the NSF with Grant No. NSF-DMR-2003117. G.T.L. thanks the projected funded by China Postdoctoral Science Foundation (Grant no. 2019M661474) and the National Science Foundation of China (12004243). The computations in this paper were run on the π 2.0 cluster supported by the Center for High Performance Computing at Shanghai Jiao Tong University.

REFERENCES

- (1) Bai, Y.; Siponkoski, T.; Peräntie, J., *et al.* Ferroelectric, pyroelectric, and piezoelectric properties of a photovoltaic perovskite oxide. *Applied Physics Letters* **2017**, 110.
- (2) Bouhemadou, A.; Haddadi, K. Structural, elastic, electronic and thermal properties of the cubic perovskite-type BaSnO₃. *Solid State Sciences* **2010**, 12, 630-636.
- (3) Giustino, F. Electron-phonon interactions from first principles. *Reviews of Modern Physics* **2017**, 89, 015003.
- (4) Peter, Y.; Cardona, M., *Fundamentals of semiconductors: physics and materials properties*. Springer Science & Business Media: 2010.
- (5) Zhang, Y.; Wang, J.; Sahoo, M., *et al.* Strain-induced ferroelectricity and lattice coupling in BaSnO₃ and SrSnO₃. *Physical Chemistry Chemical Physics* **2017**, 19, 26047-26055.
- (6) Shockley, W.; Bardeen, J. Energy bands and mobilities in monatomic semiconductors. *Physical Review* **1950**, 77, 407.
- (7) Bardeen, J.; Shockley, W. Deformation potentials and mobilities in non-polar crystals. *Physical review* **1950**, 80, 72.
- (8) Franchini, C.; Reticcioli, M.; Setvin, M., *et al.* Polarons in materials. *Nature Reviews Materials* **2021**, 1-27.
- (9) Cohen, R. E. Origin of ferroelectricity in perovskite oxides. *Nature* **1992**, 358, 136-138.
- (10) Ong, K. P.; Fan, X.; Subedi, A., *et al.* Transparent conducting properties of SrSnO₃ and ZnSnO₃. *APL Materials* **2015**, 3.
- (11) Singh, D. J.; Xu, Q.; Ong, K. P. Strain effects on the band gap and optical properties of perovskite SrSnO₃ and BaSnO₃. *Applied Physics Letters* **2014**, 104, 011910.
- (12) Wang, T.; Prakash, A.; Dong, Y., *et al.* Engineering SrSnO₃ phases and electron mobility at room temperature using epitaxial strain. *ACS applied materials & interfaces* **2018**, 10, 43802-43808.
- (13) Bellal, B.; Hadjarab, B.; Bouguelia, A., *et al.* Visible light photocatalytic reduction of water using SrSnO₃ sensitized by CuFeO₂. *Theoretical and Experimental Chemistry* **2009**, 45, 172-179.
- (14) Shannon, R. D. Revised effective ionic radii and systematic studies of interatomic distances in halides and chalcogenides. *Acta crystallographica section A: crystal physics, diffraction, theoretical and general crystallography* **1976**, 32, 751-767.
- (15) Smith, M. G.; Goodenough, J. B.; Manthiram, A., *et al.* Tin and antimony valence states in

BaSn_{0.85}Sb_{0.15}O₃– δ . *Journal of Solid State Chemistry* **1992**, 98, 181-186.

(16) Petersen, A.; Bhattacharya, S.; Tritt, T. M., *et al.* Critical analysis of lattice thermal conductivity of half-Heusler alloys using variations of Callaway model. *Journal of Applied Physics* **2015**, 117, 035706.

(17) Roufousse, M. C.; Klemens, P. G. Lattice thermal conductivity of minerals at high temperatures. *Journal of Geophysical Research* **1974**, 79, 703-705.

(18) Yadav, K.; Singh, S.; Muthuswamy, O., *et al.* Unravelling the phonon scattering mechanism in Half-Heusler alloys ZrCo_{1-x}Ir_xSb (x= 0, 0.1, and 0.25). *arXiv preprint arXiv:2107.11567* **2021**.

(19) Xu, C.; Wang, C.; Yu, J., *et al.* Structure and optical properties of Er-doped CaO-Al₂O₃ (Ga₂O₃) glasses fabricated by aerodynamic levitation. *Journal of the American Ceramic Society* **2017**, 100, 2852-2858.

(20) Liu, H.-R.; Yang, J.-H.; Xiang, H. J., *et al.* Origin of the superior conductivity of perovskite Ba(Sr)SnO₃. *Applied Physics Letters* **2013**, 102.

(21) Smirnova, I. S.; Bazhenov, A. V.; Fursova, T. N., *et al.* IR-active optical phonons in Pnma-1, Pnma-2 and phases of. *Physica B: Condensed Matter* **2008**, 403, 3896-3902.

(22) Kreisel, J.; Glazer, A.; Jones, G., *et al.* An x-ray diffraction and Raman spectroscopy investigation of A-site substituted perovskite compounds: the (Na_{1-x}K_x)_{0.5}BiO₃·5TiO₃ (0 < x < 1) solid solution. *Journal of Physics: Condensed Matter* **2000**, 12, 3267.

(23) Li, W.; Shen, Z.; Feng, Z., *et al.* Temperature dependence of Raman scattering in hexagonal gallium nitride films. *Journal of Applied Physics* **2000**, 87, 3332-3337.

(24) Balkanski, M.; Wallis, R. F.; Haro, E. Anharmonic effects in light scattering due to optical phonons in silicon. *Physical Review B* **1983**, 28, 1928-1934.

(25) Kim, H. J.; Kim, J.; Kim, T. H., *et al.* Indications of strong neutral impurity scattering in Ba(Sn,Sb)O₃ single crystals. *Physical Review B* **2013**, 88.

(26) Zhang, Y.; Wu, X. Vanadium sulfide nanoribbons: Electronic and magnetic properties. *Physics Letters A* **2013**, 377, 3154-3157.

(27) Kresse, G.; Furthmüller, J. Efficient iterative schemes for ab initio total-energy calculations using a plane-wave basis set. *Physical review B* **1996**, 54, 11169.

(28) Perdew, J. P.; Wang, Y. Accurate and simple analytic representation of the electron-gas correlation energy. *Physical review B* **1992**, 45, 13244.

(29) Ceperley, D. M.; Alder, B. J. Ground state of the electron gas by a stochastic method. *Physical review letters* **1980**, 45, 566.

(30) Heyd, J.; Scuseria, G. E.; Ernzerhof, M. Hybrid functionals based on a screened Coulomb potential. *The Journal of chemical physics* **2003**, 118, 8207-8215.

(31) Paier, J.; Marsman, M.; Hummer, K., *et al.* Screened hybrid density functionals applied to solids. *The Journal of chemical physics* **2006**, 124, 154709.

(32) Bjaalie, L.; Himmetoglu, B.; Weston, L., *et al.* Oxide interfaces for novel electronic applications. *New Journal of Physics* **2014**, 16, 025005.

(33) Grüneis, A.; Kresse, G.; Hinuma, Y., *et al.* Ionization potentials of solids: the importance of vertex corrections. *Physical review letters* **2014**, 112, 096401.